PIXWORLD: UNIFYING 3D SCENE GENERATION AND RECONSTRUCTION IN PIXEL SPACE

Sensen Gao[1*], **Zhaoqing Wang**[2*], **Qihang Cao**[1], **Dongdong Yu**[2], **Changhu Wang**[2], **Jia-Wang Bian**[2†]
[1] Nanyang Technological University [2] AISphere
* Co-first authors. †Corresponding authors.

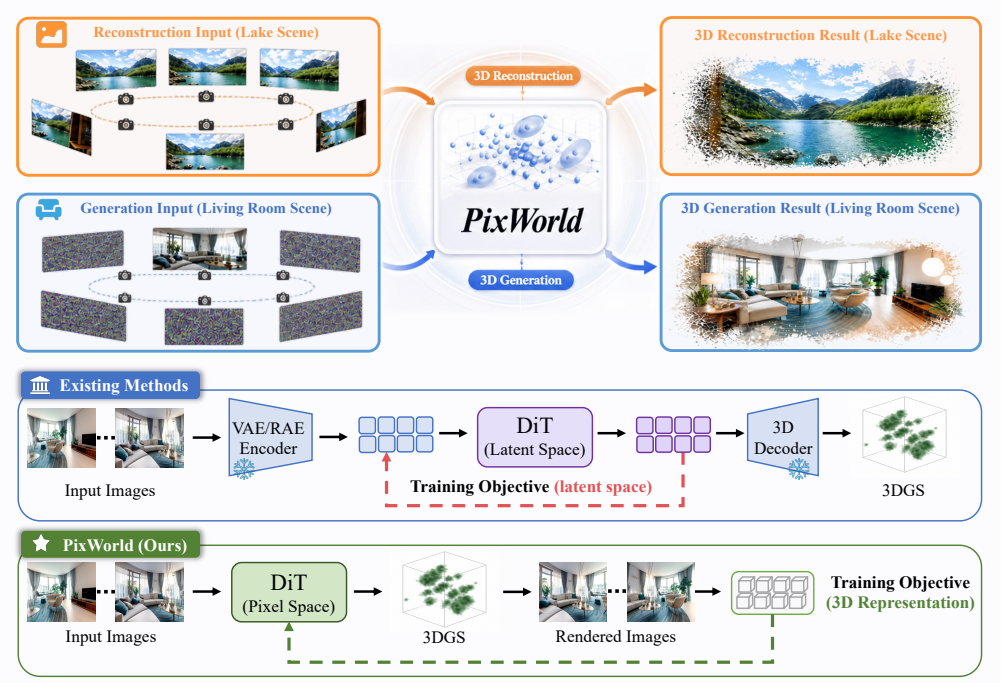

Figure 1: PixWorld unifies 3D scene reconstruction and generation within a single model. Unlike prior approaches that compute losses in the latent space of a VAE (Kingma & Welling, 2013) or RAE (Zheng et al., 2025), PixWorld applies a flow matching objective directly in pixel space over multi-view renderings, enabling end-to-end optimization of the underlying 3D representation. This design avoids the information loss inherent to latent representations and eliminates the cost of pretraining a VAE or RAE.

ABSTRACT

3D reconstruction and generation are commonly tackled by separate paradigms: pixel-based regression for reconstruction, and latent diffusion for generation. Recent works attempt to unify them in latent space, but with notable drawbacks: the diffusion objective is defined on latent features rather than the underlying 3D representation, and both branches suffer from information loss introduced by latent encoding, while requiring a pretrained Variational Autoencoder (VAE) or Representation Autoencoder (RAE). In this paper, we reformulate these two tasks under a unified pixel-space diffusion paradigm and introduce PixWorld, a single model that jointly addresses 3D reconstruction and generation. By supervising diffusion directly on rendered images, PixWorld removes the above limitations and aligns optimization with 3D scene fidelity. Beyond photometric and perceptual supervision that operates at the 2D image level and lacks 3D geometric awareness, we further introduce a geometry perception loss that aligns rendered views with their ground truth in the geometry-aware feature space of a pretrained 3D foundation model, providing 3D structural supervision. PixWorld consistently outperforms

prior latent-space generation methods and matches state-of-the-art reconstruction methods, demonstrating the superiority of a unified pixel-space approach.

1 INTRODUCTION

Building 3D scenes from visual observations is a long-standing goal in computer vision, with broad impact across gaming, robotics, embodied AI, and VR/AR (Ding et al., 2025; Kong et al., 2025; Ye et al., 2026b; Zhang et al., 2025). Two complementary directions have driven progress in this space: reconstruction recovers 3D scenes from real-world captures, while generation synthesizes plausible scenes from limited or even imagined conditions (Zhang et al., 2025; Wang et al., 2026; Li et al., 2026). Together, they form the technological foundation for populating the digital worlds of tomorrow.

3D scene generation and reconstruction have long developed as two separate lines of research. Reconstruction is dominated by feed-forward methods that regress 3D representations directly from multi-view images (Hong et al., 2023; Charatan et al., 2024; Szymanowicz et al., 2024; Xu et al., 2025; Chen et al., 2024a). Generation has evolved from per-scene optimization with 2D priors via score distillation (Lin et al., 2023; Poole et al., 2022; Tang et al., 2023; Wang et al., 2023) to latent-space diffusion as the current mainstream (Yang et al., 2025; Go et al., 2025b; Huang et al., 2026; Li et al., 2025b), with recent extensions diffusing in the feature space of pretrained 3D foundation models or representation autoencoders (Gao et al., 2026; Sun et al., 2026; Jang et al., 2026). A recent work, Gen3R (Huang et al., 2026), attempts to unify the two tasks by extending the latent-space generation pipeline to also handle reconstruction. However, this design introduces clear limitations: the diffusion objective is defined on intermediate latent features rather than the underlying 3D representation, preventing the 3D output from being directly optimized; in addition, both branches suffer from information loss introduced by the pretrained Variational Autoencoder (VAE) or Representation Autoencoder (RAE), which itself requires additional training.

To address these limitations, we reformulate unification under a pixel-space diffusion paradigm and introduce PixWorld, a single framework that jointly handles 3D reconstruction and generation. This design brings two key benefits. First, for both generation and reconstruction, eliminating the latent stage removes the information loss introduced by latent encoding and the additional training cost of a VAE/RAE, which is especially critical for reconstruction as a fidelity-bound task. Second, for generation, the diffusion objective directly supervises the 3D representation through differentiable rendering (see Fig. 1), aligning the training signal with the fidelity of the 3D scene rather than with targets in an intermediate latent space. Building on this pixel-space framework, the unification reduces to how to expose both tasks to a single forward pass. We achieve this by partitioning multi-view inputs into clean and noisy subsets: clean views drive reconstruction, while noisy ones are generated conditioned on the clean ones, with both producing a pixel-aligned 3D Gaussian representation (Kerbl et al., 2023).

Despite this direct pixel-space supervision, image-level photometric and perceptual losses do not fully guarantee geometrically faithful 3D structure. To address this, we introduce a geometry perception loss that brings rendered views and their ground-truth counterparts close in the geometry-aware feature space of a pretrained 3D foundation model. As this feature space encodes 3D geometric structure beyond 2D appearance, the loss directly encourages the rendered scene to share the same underlying geometry as the ground truth. Extensive experiments on RealEstate10K (Zhou et al., 2018), DL3DV (Ling et al., 2024) and WorldScore (Duan et al., 2025) demonstrate that a single PixWorld model delivers high-fidelity 3D scene generation and reconstruction, matching state-of-the-art reconstruction methods while outperforming previous latent-space generation approaches.

Our main contributions are summarized as follows:

- We propose PixWorld, an end-to-end pixel-space diffusion framework that supervises a pixel-aligned 3D Gaussian representation directly through multi-view differentiable rendering, with no intermediate VAE or RAE. This eliminates the information loss and training cost of a latent autoencoder, aligns the diffusion signal with the fidelity of the 3D scene itself, and naturally unifies 3D scene generation and reconstruction in a single model.

- We introduce a geometry perception loss that aligns rendered views with ground truth in the geometry-aware feature space of a pretrained 3D foundation model, providing 3D structural supervision beyond 2D photometric and perceptual losses.
- Experiments show that a single PixWorld model achieves superior performance on both 3D scene generation and reconstruction, establishing pixel-space diffusion as a unified paradigm for 3D scene modeling.

2 Related Work

2.1 3D Scene Generation

Diffusion-based Iterative 3D Scene Generation. Early 3D generation methods leverage pretrained 2D generative models (Rombach et al., 2022; Podell et al., 2023; Zhang et al., 2023; Peebles & Xie, 2023) as generative priors. A representative line employs Score Distillation Sampling (SDS) (Lin et al., 2023; Poole et al., 2022; Tang et al., 2023; Wang et al., 2023) to optimize a 3D representation such as 3DGS (Kerbl et al., 2023) or NeRF (Mildenhall et al., 2021) by aligning rendered views with a pretrained 2D diffusion model. Without explicit multi-view constraints, these methods suffer from cross-view inconsistency, and the per-scene iterative optimization further limits their scalability.

Multi-View Reconstruction-Based 3D Scene Generation. A second line first synthesizes multi-view images or videos with pretrained 2D diffusion models, then performs 3D reconstruction from the synthesized views (Chen et al., 2024b; Gao et al., 2024; Hao et al., 2025; Liu et al., 2024; 2023; Sargent et al., 2023; Shi et al., 2023; Sun et al., 2024; Wu et al., 2024; Zhao et al., 2024) or incremental outpainting (Chung et al., 2023; Fridman et al., 2023; Schwarz et al., 2025; Yu et al., 2024; 2025a). While avoiding per-scene optimization, these methods rely on 2D RGB priors without explicit 3D reasoning, often resulting in inconsistent geometry and weak multi-view fidelity.

3D Scene Generation in Latent Spaces. More recent work moves diffusion into compressed latent spaces and learns a latent-to-3D decoder, typically targeting 3DGS. One line freezes a pretrained image or video VAE (*e.g.*, SD-VAE (Podell et al., 2023), Wan-VAE (Wan et al., 2025)) and trains a decoder that maps the resulting latents to 3D Gaussians, with a diffusion backbone fine-tuned in this latent space (Yang et al., 2025; Go et al., 2025b; Li et al., 2024; 2025b; Dai et al., 2025; Go et al., 2025c;a; Zhou et al., 2026; Wang et al., 2025b). Following the shift from VAEs to Representation Autoencoders (RAEs) (Zheng et al., 2025; Shi et al., 2025; Chen et al., 2025a; Bi et al., 2025), a more recent line operates in the representation space of pretrained 3D foundation models (Gao et al., 2026; Sun et al., 2026; Jang et al., 2026). Building on this latent-space paradigm, Gen3R (Huang et al., 2026) further attempts to unify reconstruction and generation within a single latent-space model.

2.2 3D Scene Reconstruction

3D scene reconstruction aims to recover 3D representations from one or more captured views. Classical pipelines rely on multi-view stereo and structure-from-motion to estimate dense geometry, while NeRF (Mildenhall et al., 2021) and 3D Gaussian Splatting (Kerbl et al., 2023) popularized per-scene optimization for high-fidelity novel view synthesis. To avoid expensive per-scene fitting, recent feed-forward methods learn to directly map sparse or dense multi-view inputs to a 3D representation in a single forward pass (Hong et al., 2023; Charatan et al., 2024; Szymanowicz et al., 2024; Chen et al., 2024a; Xu et al., 2025), with LRM (Hong et al., 2023) regressing implicit triplanes and pixel-aligned Gaussian regressors (Charatan et al., 2024; Szymanowicz et al., 2024; Chen et al., 2024a) predicting per-pixel Gaussians. These methods are deterministic and conditioned on the available observations, and therefore cannot synthesize unseen content beyond the input views.

2.3 Pixel-Space Generation

Latent diffusion models (Rombach et al., 2022; Podell et al., 2023; Peebles & Xie, 2023) dominate large-scale image generation by operating in a compressed VAE latent space, introducing an indirection between the generative target and the pixel output. A complementary line of work performs diffusion directly in pixel space (Dhariwal & Nichol, 2021; Jabri et al., 2023; Hoogeboom et al., 2023; 2025; Wang et al., 2025c; Chen et al., 2025c; Yu et al., 2025b; Ma et al., 2025; Chen et al., 2025d; Li & He, 2025), showing that, with sufficient capacity and data, pixel-space generation can

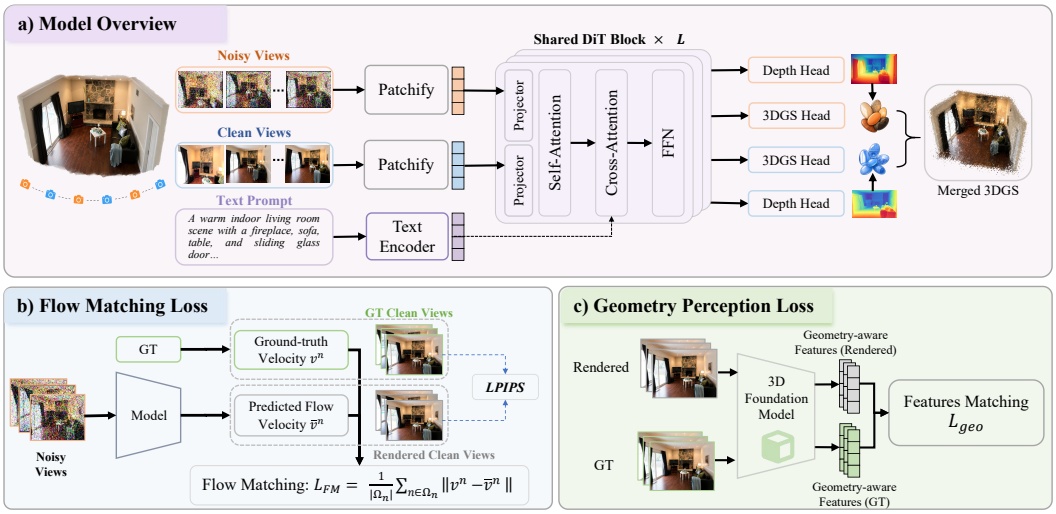

Figure 2: **Overview of PixWorld.** (a) PixWorld adopts a unified DiT-based framework that takes noisy and clean multi-view inputs, with optional text conditioning, and jointly predicts depth and 3DGS through shared transformer blocks. (b) A pixel-space flow matching loss is imposed on rendered multi-view images to directly optimize the underlying 3D representation. (c) A geometry perception loss further enforces structural consistency by aligning rendered views with ground-truth observations through a 3D foundation model.

match or surpass its latent-space counterparts in fidelity. We extend this perspective to the 3D setting: by performing diffusion directly in pixel space, PixWorld removes the intermediate VAE/RAE of prior latent-space 3D methods and supervises the 3D representation directly through differentiable rendering of the predicted 3DGS.

3 Methodology

We present PixWorld, a unified pixel-space diffusion framework that jointly addresses 3D scene reconstruction and generation within a single model (Fig. 2). Given a set of posed multi-view images, PixWorld partitions them into a clean subset and a noisy subset, jointly processes both with a two-stream diffusion transformer, and decodes the resulting features into a pixel-aligned 3D Gaussian representation (Kerbl et al., 2023). The predicted Gaussians are rendered back to images, on which the diffusion objective is supervised directly, aligning optimization with 3D scene fidelity rather than with targets in an intermediate latent space. To further provide 3D structural supervision beyond photometric and perceptual losses that operate at the 2D image level, we introduce a geometry perception loss defined in the geometry-aware feature space of a pretrained 3D foundation model.

3.1 Preliminary: Pixel-Space Diffusion

We first briefly review diffusion in the standard 2D image setting and contrast pixel-space diffusion with latent-space diffusion. In latent diffusion, an image x is first mapped into a compact latent representation by a pretrained image autoencoder, *e.g.*, a VAE or a RAE, written as $\mathcal{E}_{\mathrm{AE}} : x \mapsto z$. Diffusion is then performed in the latent space, and the denoised latent is finally mapped back to RGB space by $\mathcal{D}_{\mathrm{AE}} : \hat{z} \mapsto \hat{x}$. This design reduces the dimensionality and computational cost of diffusion modeling, but it also inserts an intermediate autoencoding bottleneck between the diffusion variable and the final image-space supervision.

Following JiT (Li & He, 2025), we instead adopt *image prediction* in pixel space. Given a clean image $x \in \mathbb{R}^{H\times W\times 3}$, a Gaussian noise sample $\epsilon \sim \mathcal{N}(\mathbf{0}, \mathbf{I})$, and a timestep $t \in [0, 1]$, the noisy input is constructed by linear interpolation, $x_t = t\,x + (1-t)\,\epsilon$. The denoiser is parameterized directly as an image predictor,

$$f_\theta : (x_t, t, c) \mapsto \hat{x}, \tag{1}$$

where c denotes conditional information such as class labels or text embeddings. The predicted image is converted into a velocity field $\hat{v} = (\hat{x} - x_t)/(1-t)$, yielding the flow-matching objective

$$\mathcal{L}_{\mathrm{FM}} = \mathbb{E}_{x,\epsilon,t}\left[\|\hat{v} - v\|_2^2\right] = \mathbb{E}_{x,\epsilon,t}\left[\frac{\|\hat{x} - x\|_2^2}{(1-t)^2}\right], \tag{2}$$

where $v = x - \epsilon$ is the ground-truth velocity. This pixel-space parameterization is particularly attractive for our 3D setting. Latent diffusion defines its objective on encoded latents, leaving the diffusion process decoupled from both the rendered output and the underlying 3D representation it is meant to supervise. Pixel-space diffusion instead keeps the diffusion variable and the rendered output in the same RGB domain, so the diffusion objective can be supervised directly on rendered images, aligning optimization with 3D scene fidelity rather than with targets in an intermediate latent space.

3.2 PIXWORLD FRAMEWORK

Task formulation. Building on the 2D pixel-space diffusion formulation above, PixWorld extends image prediction to a posed multi-view setting. Given a scene with N posed views, we denote the RGB images and camera parameters by $\mathcal{I} = \{\mathcal{I}^n\}_{n=1}^N, \mathcal{T} = \{\mathcal{T}^n\}_{n=1}^N$, where $\mathcal{I}^n \in \mathbb{R}^{H\times W\times 3}$ is the RGB image of the n-th view and $\mathcal{T}^n$ denotes its camera parameters. We partition the view indices into a clean subset Ω_{c} and a noisy subset Ω_{n} such that

$$\Omega_{\mathrm{c}} \cup \Omega_{\mathrm{n}} = \{1, \ldots, N\}, \qquad \Omega_{\mathrm{c}} \cap \Omega_{\mathrm{n}} = \varnothing, \qquad |\Omega_{\mathrm{c}}| \geq 1. \tag{3}$$

When $\Omega_{\mathrm{n}} = \varnothing$, the task reduces to multi-view 3D reconstruction from clean observations. Otherwise, PixWorld predicts the noisy views conditioned on the clean ones. An optional text prompt y may further specify the scene.

For each view n, the model input is defined as

$$\tilde{\mathcal{I}}_t^n = \begin{cases} \mathcal{I}^n, & n \in \Omega_{\mathrm{c}}, \\ t\,\mathcal{I}^n + (1-t)\epsilon^n, & n \in \Omega_{\mathrm{n}}, \end{cases} \qquad \epsilon^n \sim \mathcal{N}(\mathbf{0}, \mathbf{I}), \tag{4}$$

where all noisy views of the same scene share the same timestep t. We denote the mixed multi-view input by $\tilde{\mathcal{I}}_t = \{\tilde{\mathcal{I}}_t^n\}_{n=1}^N$.

Two-stream diffusion transformer. Given the mixed input $\tilde{\mathcal{I}}_t$, PixWorld uses a two-stream diffusion transformer

$$f_\theta : (\tilde{\mathcal{I}}_t, \mathcal{T}, y) \mapsto (\hat{\mathcal{D}}, \hat{\mathcal{G}}), \tag{5}$$

where $\hat{\mathcal{D}} = \{\hat{\mathcal{D}}^n\}_{n=1}^N$ denotes the predicted multi-view depth maps and $\hat{\mathcal{G}}$ denotes the predicted pixel-aligned 3D Gaussian scene representation. Clean and noisy views are embedded by separate input projections and jointly processed by shared transformer blocks. The noisy stream is conditioned on the sampled timestep t, while the clean stream always receives the fully denoised time embedding corresponding to $t = 1$. Camera parameters are injected via PRoPE (Li et al., 2025a), and the optional text condition is fused through cross-attention.

3D Gaussian decoding and rendering. From the shared features, the network predicts a depth map $\hat{\mathcal{D}}^n$ for each view together with the Gaussian attributes that define $\hat{\mathcal{G}}$. Rather than regressing 3D centers directly, we unproject each pixel using its predicted depth and camera: for the p-th pixel of the n-th view with depth $\hat{d}_p^n$, the Gaussian center is $\mu_p^n = \Pi^{-1}(p, \hat{d}_p^n, \mathcal{T}^n)$, where Π^{-1} is the inverse projection to world space. Aggregating across all pixels and views yields the scene-level representation $\hat{\mathcal{G}}$, which is rendered by a differentiable renderer $\mathcal{R} : (\hat{\mathcal{G}}, \mathcal{T}^n) \mapsto \bar{\mathcal{I}}^n$, giving the rendered multi-view set $\bar{\mathcal{I}} = \{\bar{\mathcal{I}}^n\}_{n=1}^N$.

FM rendering and depth objectives. To align the rendering supervision with the velocity-based parameterization introduced in Section 3.1, we formulate the rendering loss in the same FM style. For each noisy view $n \in \Omega_{\mathrm{n}}$, we define the rendered and ground-truth velocities as $\bar{v}^n = (\bar{\mathcal{I}}^n - \tilde{\mathcal{I}}_t^n)/(1-t)$ and $v^n = (\mathcal{I}^n - \tilde{\mathcal{I}}_t^n)/(1-t)$, where $v^n = \mathcal{I}^n - \epsilon^n$ follows directly from Eq. equation 4. For each

clean view $n \in \Omega_{\mathrm{c}}$, the rendered image $\bar{\mathcal{I}}^n$ is supervised against the observation $\mathcal{I}^n$ by a direct MSE term, since clean views serve as noise-free reconstruction anchors. We then define

$$\mathcal{L}_{\mathrm{render}} = \underbrace{\frac{1}{|\Omega_{\mathrm{c}}|} \sum_{n \in \Omega_{\mathrm{c}}} \|\bar{\mathcal{I}}^n - \mathcal{I}^n\|_2^2}_{\mathcal{L}_{\mathrm{recon}}} + \underbrace{\frac{\mathbf{1}[\,|\Omega_{\mathrm{n}}| > 0\,]}{|\Omega_{\mathrm{n}}|} \sum_{n \in \Omega_{\mathrm{n}}} \|\bar{v}^n - v^n\|_2^2}_{\mathcal{L}_{\mathrm{FM}}} + \lambda_{\mathrm{lpips}}\, \mathcal{L}_{\mathrm{lpips}}, \tag{6}$$

where the FM term is equivalently written in image space as $\frac{1}{|\Omega_{\mathrm{n}}|} \sum_{n \in \Omega_{\mathrm{n}}} \frac{\|\bar{\mathcal{I}}^n - \mathcal{I}^n\|_2^2}{(1-t)^2}$, and the perceptual term is defined as $\mathcal{L}_{\mathrm{lpips}} = \mathbf{1}[t > t_{\mathrm{th}}]\, \frac{1}{N} \sum_{n=1}^{N} \mathrm{LPIPS}(\bar{\mathcal{I}}^n, \mathcal{I}^n)$. The indicator $\mathbf{1}[\,|\Omega_{\mathrm{n}}| > 0\,]$ disables the FM term in the pure reconstruction case ($\Omega_{\mathrm{n}} = \varnothing$), while $|\Omega_{\mathrm{c}}| \geq 1$ is guaranteed by Eq. equation 3. We activate the LPIPS term only when $t > t_{\mathrm{th}}$, since perceptual supervision is unreliable when the noisy input is too close to pure noise. We further sample 4–8 novel views per iteration and supervise their renderings against ground-truth images via MSE and lpips loss, regularizing the 3DGS to render well from all viewpoints.

We further supervise the predicted depth maps against pseudo-depth labels $\mathcal{D}^\star = \{\mathcal{D}^{\star n}\}_{n=1}^N$ (obtained from DA3 (Lin et al., 2025)) by

$$\mathcal{L}_{\mathrm{depth}} = \frac{1}{N} \sum_{n=1}^{N} \rho\Big(\log \hat{\mathcal{D}}^{\,n} - \log \mathcal{D}^{\star n}\Big), \tag{7}$$

where $\rho(\cdot)$ is a Huber loss applied element-wise and then averaged over pixels.

3.3 Geometry Perception Loss

Motivation. Although $\mathcal{L}_{\mathrm{render}}$ enforces view consistency, it remains photometric in nature and therefore does not fully constrain the underlying 3D structure. In particular, depth may drift along a viewing ray as long as the projected appearance is preserved, translucent floaters may average to plausible colors, and view-dependent texture can partially compensate for geometric misalignment. These ambiguities are especially problematic for noisy views, which do not have direct clean image supervision at the input stage.

To complement pixel-level supervision with a more structural signal, we introduce a *geometry perception loss* defined in the feature space of a frozen 3D foundation model Ψ (*e.g.*, VGGT (Wang et al., 2025a) or π^3 (Wang et al., 2025d)).

Geometry perception loss. Given the rendered view set $\bar{\mathcal{I}}$ and the ground-truth view set $\mathcal{I}$ under the same cameras $\mathcal{T}$, we extract multi-view geometric features with $\Psi : (\mathcal{I}, \mathcal{T}) \mapsto \mathcal{H} \in \mathbb{R}^{N \times C_\Psi \times H' \times W'}$. Applying Ψ to the rendered and reference images gives

$$\bar{\mathcal{H}} = \Psi(\bar{\mathcal{I}}, \mathcal{T}) = \{\bar{\mathcal{H}}^n\}_{n=1}^N, \qquad \mathcal{H}^\star = \Psi(\mathcal{I}, \mathcal{T}) = \{\mathcal{H}^{\star n}\}_{n=1}^N, \tag{8}$$

where $\bar{\mathcal{H}}^n$ and $\mathcal{H}^{\star n}$ denote the rendered and reference feature maps of the n-th view, respectively. We minimize the average per-location cosine distance between the two feature fields only when the timestep is sufficiently large:

$$\mathcal{L}_{\mathrm{geo}} = \mathbf{1}[t > t_{\mathrm{th}}]\, \frac{1}{NH'W'} \sum_{n=1}^{N} \sum_{p} \left[1 - \frac{\langle \bar{h}_p^{\,n},\, h_p^{\star n} \rangle}{\|\bar{h}_p^{\,n}\|_2\, \|h_p^{\star n}\|_2}\right], \tag{9}$$

where $\bar{h}_p^{\,n}$ and $h_p^{\star n}$ are the feature vectors at location p of $\bar{\mathcal{H}}^n$ and $\mathcal{H}^{\star n}$, respectively. Because Ψ jointly processes all views together with their cameras, its features encode cross-view 3D structure rather than only per-image appearance. Consequently, two renderings that are individually photo-consistent but mutually inconsistent in 3D can still produce different feature maps and incur a large $\mathcal{L}_{\mathrm{geo}}$. During training, we freeze Ψ, stop gradients on the reference branch $\mathcal{H}^\star$, and back-propagate only through the rendered branch $\bar{\mathcal{H}}$, so that Ψ acts purely as a structural critic. We activate this term only when $t > t_{\mathrm{th}}$, since geometric feature matching is unstable when the noisy input is too close to pure noise.

Overall objective. The full training objective is $\mathcal{L} = \mathcal{L}_{\mathrm{render}} + \lambda_{\mathrm{depth}}\, \mathcal{L}_{\mathrm{depth}} + \lambda_{\mathrm{geo}}\, \mathcal{L}_{\mathrm{geo}}$.

Table 1: **Quantitative comparison of novel-view synthesis** on RealEstate10K (Zhou et al., 2018) and DL3DV-10K (Ling et al., 2024) under 4-view and 8-view input settings. Best results are in **bold**; second best are underlined.

	RealEstate10K						DL3DV-10K					
	4-views			8-views			4-views			8-views		
Method	PSNR↑	SSIM↑	LPIPS↓	PSNR↑	SSIM↑	LPIPS↓	PSNR↑	SSIM↑	LPIPS↓	PSNR↑	SSIM↑	LPIPS↓
MVSplat (Chen et al., 2024a)	22.58	0.762	0.264	21.64	0.719	0.301	17.11	0.501	0.410	15.75	0.432	0.491
DepthSplat (Xu et al., 2025)	25.16	0.832	0.194	27.77	0.872	0.154	20.38	**0.719**	0.320	19.26	**0.692**	0.360
AnySplat (Jiang et al., 2025)	20.07	0.731	0.286	20.52	0.752	0.262	20.11	0.671	0.318	20.02	0.664	0.327
YoNoSplat (Ye et al., 2026a)	25.86	0.841	0.143	28.35	0.889	0.107	22.89	0.710	0.228	21.92	0.678	0.262
PixWorld (Ours)	**26.21**	**0.844**	**0.138**	**28.58**	**0.892**	**0.101**	**23.18**	0.714	**0.226**	**22.46**	0.681	**0.257**

Table 2: **Quantitative comparison on single-image 3D scene generation, averaged.** Results on RealEstate10K (Zhou et al., 2018) and DL3DV-10K (Ling et al., 2024) under the 1-view setting, averaged over First Frame and Bidirectional configurations. Best in **bold**; second best underlined.

	Novel View Synthesis			*Generation Quality*				*Camera Control*		
Method	PSNR↑	SSIM↑	LPIPS↓	I2V Subj.↑	I2V BG↑	I.Q.↑	Aes.Q.↑	AUC@30↑	AUC@15↑	AUC@5↑
RealEstate10K										
LVSM (Jin et al., 2025)	17.82	0.603	0.336	0.971	0.970	0.593	0.506	0.710	0.592	0.372
GF (Wu et al., 2025)	15.63	0.553	0.454	0.931	0.941	0.504	0.475	0.596	0.478	0.290
Gen3C (Ren et al., 2025)	17.26	0.624	0.391	0.951	0.956	0.561	0.524	0.648	0.514	0.334
FlashWorld (Li et al., 2025b)	16.51	0.626	0.403	0.958	0.960	0.615	0.550	0.843	0.758	0.546
Gen3R (Huang et al., 2026)	17.59	0.631	0.382	0.974	0.971	0.552	0.536	0.633	0.433	0.147
PixWorld (Ours)	**18.88**	**0.702**	**0.325**	**0.979**	**0.978**	**0.623**	**0.556**	**0.869**	**0.798**	**0.614**
DL3DV-10K										
LVSM (Jin et al., 2025)	14.91	0.433	0.530	0.931	0.933	0.494	0.466	0.552	0.372	0.134
GF (Wu et al., 2025)	12.69	0.356	0.591	0.898	0.910	0.474	0.435	0.491	0.338	0.113
Gen3C (Ren et al., 2025)	15.58	0.514	0.479	0.927	0.933	0.532	0.496	0.552	0.377	0.128
FlashWorld (Li et al., 2025b)	15.42	0.473	0.461	0.942	0.950	0.619	0.558	0.769	0.674	0.420
Gen3R (Huang et al., 2026)	15.75	0.503	0.495	0.944	0.942	0.547	0.530	0.593	0.398	0.117
PixWorld (Ours)	**16.50**	**0.527**	**0.449**	**0.952**	**0.956**	**0.631**	**0.567**	**0.793**	**0.706**	**0.485**

4 EXPERIMENTS

4.1 TRAINING DETAILS

PixWorld has ~ 1.04B parameters and is trained from scratch on the Re10K (Zhou et al., 2018) + DL3DV-10K (Ling et al., 2024) mixture ($\sim$67K scenes in total), augmented with 10M single images from the BLIP-3o (Chen et al., 2025b) corpus that share the diffusion backbone as a 2D appearance prior. For each multi-view scene we sample $N \in \{4, \ldots, 8\}$ posed views and randomly partition them into Ω_{c} and Ω_{n}, biased toward small $|\Omega_{\mathrm{c}}|$ so that capacity is spent on conditioned generation while the all-clean case ($\Omega_{\mathrm{n}} = \varnothing$) grounds the geometry head. We use $\Psi = \pi^3$ (Wang et al., 2025d) as the frozen 3D critic for $\mathcal{L}_{\mathrm{geo}}$, and set $\lambda_{\mathrm{depth}}=1.0$ and $\lambda_{\mathrm{lpips}}=\lambda_{\mathrm{geo}}=0.1$, with the perceptual and geometric terms gated by $t > t_{\mathrm{th}}=0.3$. The model is optimized with AdamW (Loshchilov & Hutter, 2017) for $\sim$200K steps at a training resolution of 336×448 on 32 NVIDIA A800-SXM4-80G GPUs. Full architectural specifications, batching, and optimizer schedules are deferred to the Appendix B.

4.2 EVALUATION PROTOCOLS

We evaluate PixWorld on four protocols covering 3D reconstruction and 3D scene generation (see Fig. 3). For RealEstate10K (Zhou et al., 2018) and DL3DV-10K (Ling et al., 2024), we randomly sample 200 test scenes per dataset, restricted to clips with a large camera pose range so the protocols stress wide-baseline reasoning; for WorldScore (Duan et al., 2025) we follow the official static split (2000 scenes). For all scene-generation protocols, every baseline is conditioned on camera poses, and all baselines except LVSM (Jin et al., 2025) additionally receive a text condition. For reconstruction (Tab. 1), the model is given 4 or 8 posed views and renders held-out targets under ground-truth poses, evaluated by PSNR, SSIM (Wang et al., 2004), and LPIPS (Zhang et al., 2018). For 1-view generation (Tab. 2), the 200 scenes per dataset are split into 100 First-Frame scenes (forward trajectory generated from the first frame) and 100 Bidirectional scenes (a randomly chosen middle frame conditions generation toward both ends); 2-view generation (Tab. 3) similarly combines 100 Interpolation scenes (endpoint anchors, intermediate views generated) and 100 Extrapolation scenes (anchors at one end,

Table 3: **Quantitative comparison on two-view 3D scene generation, averaged.** Results on RealEstate10K (Zhou et al., 2018) and DL3DV-10K (Ling et al., 2024) under the 2-view setting, averaged over Interpolation and Extrapolation configurations. Best in **bold**; second best underlined.

	Novel View Synthesis			*Generation Quality*				*Camera Control*		
Method	PSNR↑	SSIM↑	LPIPS↓	I2V Subj.↑	I2V BG↑	I.Q.↑	Aes.Q.↑	AUC@30↑	AUC@15↑	AUC@5↑
RealEstate10K										
LVSM (Jin et al., 2025)	**23.61**	**0.819**	0.215	0.970	0.964	0.607	0.516	0.861	0.788	0.611
GF (Wu et al., 2025)	18.27	0.647	0.353	0.925	0.939	0.507	0.464	0.630	0.473	0.223
Gen3C (Ren et al., 2025)	20.12	0.714	0.300	0.948	0.947	0.567	0.518	0.698	0.538	0.255
FlashWorld (Li et al., 2025b)	21.48	0.770	0.257	0.964	0.962	0.619	0.547	0.877	0.811	0.637
Gen3R (Huang et al., 2026)	21.33	0.724	0.283	0.970	0.972	0.550	0.540	0.728	0.576	0.258
PixWorld (Ours)	23.54	0.815	**0.210**	**0.974**	**0.974**	**0.628**	**0.561**	**0.880**	**0.817**	**0.649**
DL3DV-10K										
LVSM (Jin et al., 2025)	19.18	0.589	0.343	0.915	0.917	0.533	0.502	0.740	0.609	0.374
GF (Wu et al., 2025)	15.38	0.459	0.470	0.897	0.912	0.479	0.445	0.563	0.379	0.147
Gen3C (Ren et al., 2025)	17.62	0.542	0.412	0.927	0.934	0.536	0.502	0.627	0.433	0.176
FlashWorld (Li et al., 2025b)	18.27	0.562	0.359	0.938	0.948	0.600	0.558	0.802	0.714	0.514
Gen3R (Huang et al., 2026)	18.05	0.558	0.392	0.942	0.944	0.535	0.530	0.726	0.560	0.245
PixWorld (Ours)	**19.37**	**0.594**	**0.340**	**0.950**	**0.956**	**0.607**	**0.565**	**0.821**	**0.734**	**0.534**

Table 4: **Quantitative comparison on the WorldScore benchmark (Duan et al., 2025).** We report all seven official metrics together with their average. **Bold** and underline indicate the best and the second-best results, respectively.

Method	Camera Control	Object Control	Content Alignment	3D Consistency	Photometric Consistency	Style Consistency	Subjective Quality	**Average**
Wan-2.1 (Wan et al., 2025)	23.53	40.32	45.44	78.74	78.36	77.18	59.38	57.56
WonderJourney (Yu et al., 2024)	84.60	37.10	35.54	80.60	79.03	62.82	**66.56**	63.75
LucidDreamer (Chung et al., 2023)	88.93	41.18	**75.00**	90.37	90.20	48.10	58.99	70.40
FlashWorld (Li et al., 2025b)	84.43	**50.28**	56.54	85.87	86.72	**79.36**	52.75	70.85
PixWorld (ours)	**91.08**	46.25	55.27	**91.39**	**93.84**	67.11	52.36	**71.04**

views generated beyond their span). For both generation settings we report three groups of metrics, each targeting one capability of a 3D world model: Novel View Synthesis (NVS) fidelity against ground-truth target views (PSNR, SSIM, LPIPS); Generation Quality from VBench (Huang et al., 2024) (I2V Subject, I2V Background, Image Quality, Aesthetic Quality), assessing perceptual realism without paired references; and Camera Control precision via π^3 (Wang et al., 2025d)-estimated AUC@$\{30°, 15°, 5°\}$ (Wang et al., 2025e) between the poses recovered from generated frames and the conditioning trajectory. On WorldScore (Tab. 4) we report all seven official metrics and their average: Camera Control and Object Control measure trajectory control fidelity, Content Alignment measures faithfulness to the text prompt, 3D and Photometric Consistency assess geometric and appearance stability across views, Style Consistency captures visual style coherence, and Subjective Quality reflects overall perceptual quality, with baseline numbers taken from the WorldScore release.

4.3 3D Scene Reconstruction

Tab. 1 reports novel-view synthesis results on RealEstate10K and DL3DV-10K under 4-view and 8-view inputs. Note that Gen3R (Huang et al., 2026), although a unified generation-and-reconstruction model, only supports point-cloud reconstruction and is therefore not directly comparable on NVS, so it is omitted here. We further note that YoNoSplat supports both a pose-free and a pose-conditioned (*with-pose*) mode; for a stronger comparison we adopt its with-pose results, which leverage ground-truth camera poses as additional input. Even against this stronger baseline, PixWorld attains the best PSNR and LPIPS across all settings, as well as the best SSIM on RealEstate10K, trailing only DepthSplat on SSIM for DL3DV-10K. Concretely, PixWorld consistently improves PSNR over YoNoSplat on both RealEstate10K and DL3DV-10K (4/8 views), and lowers LPIPS in every case (*e.g.*, 0.138 vs. 0.143 at 4-view RealEstate10K). These results show that our pixel-space formulation and geometry-aware supervision yield stronger cross-view consistency and more accurate 3D reconstruction.

Figure 3: **Visualization of PixWorld under different settings.** PixWorld flexibly handles both 3D reconstruction and generation: when all input views are clean, it performs reconstruction; when clean and noisy views are arbitrarily mixed, it performs generation. We visualize the camera trajectory, where blue and red frustums denote clean input views and generated views, respectively.

Table 5: **Ablation study on geometry perception loss.** We report results on RealEstate10K (Zhou et al., 2018) under the *1-view* setting.

Variant	PSNR↑	SSIM↑	LPIPS↓	I2V Subj.↑	I2V BG↑	I.Q.↑	Aes.Q.↑	AUC@30↑	AUC@15↑	AUC@5↑
Full model	19.12	0.717	0.310	0.972	0.975	0.619	0.561	0.886	0.813	0.642
w/o Geometry Perception	17.99	0.612	0.332	0.973	0.974	0.613	0.541	0.847	0.763	0.562

4.4 3D Scene Generation

We benchmark PixWorld against five representative baselines, LVSM (Jin et al., 2025), GF (Wu et al., 2025), Gen3C (Ren et al., 2025), FlashWorld (Li et al., 2025b) and Gen3R (Huang et al., 2026), on RealEstate10K (Zhou et al., 2018) and DL3DV-10K (Ling et al., 2024) under single and two-image conditioning. We report novel-view synthesis quality (PSNR, SSIM, LPIPS), VBench-style generation quality, and pose accuracy via π^3-estimated AUC at multiple thresholds. In the single-image setting (Tab. 2), averaged across First-Frame and Bidirectional trajectories, PixWorld tops every metric on both datasets, lifting PSNR by $+1.06$ dB on RealEstate10K (18.88 vs. 17.82) and $+0.75$ dB on DL3DV-10K (16.50 vs. 15.75); the gain is sharpest at strict pose thresholds, with AUC@5 rising from 0.546 to 0.614 and from 0.420 to 0.485, indicating that diffusing in pixel space and supervising through differentiable rendering yields geometrically faithful trajectories. Under two-image conditioning (Tab. 3), PixWorld again leads on perceptual, generation, and pose metrics, attaining the best LPIPS (0.210/0.340) and AUC@5 (0.649/0.534); LVSM is competitive only on raw PSNR/SSIM (gap < 0.07 dB on RealEstate10K), reflecting its deterministic regression objective. In WorldScore (Duan et al., 2025) (Tab. 4), PixWorld achieves the best overall average (71.04) and ranks first in camera controllability (91.08), 3D consistency (91.39) and photometric consistency (93.84); see Fig. 4.

4.5 Ablation Study

We ablate the geometry perception loss on RealEstate10K (Zhou et al., 2018) under the 1-view setting (Tab. 5). For a controlled comparison, we sample a 10K-sequence subset and train both variants for 30K steps under identical settings, toggling only the geometry perception loss. Removing it consistently degrades all three metric groups: PSNR drops by 1.13 dB ($19.12 \rightarrow 17.99$), SSIM by 0.105 ($0.717 \rightarrow 0.612$) and AUC@5 by 0.080 ($0.642 \rightarrow 0.562$, $\sim 12.5\%$ relative), while VBench-style scores barely shift. This pattern matches our motivation: 2D photometric and perceptual losses keep individual frames visually plausible but leave the underlying 3D geometry unsupervised, so cross-view consistency and pose fidelity suffer (see Fig. 5 in Appendix D). By aligning rendered and ground-truth views in the geometry-aware feature space of a pretrained 3D foundation model, our

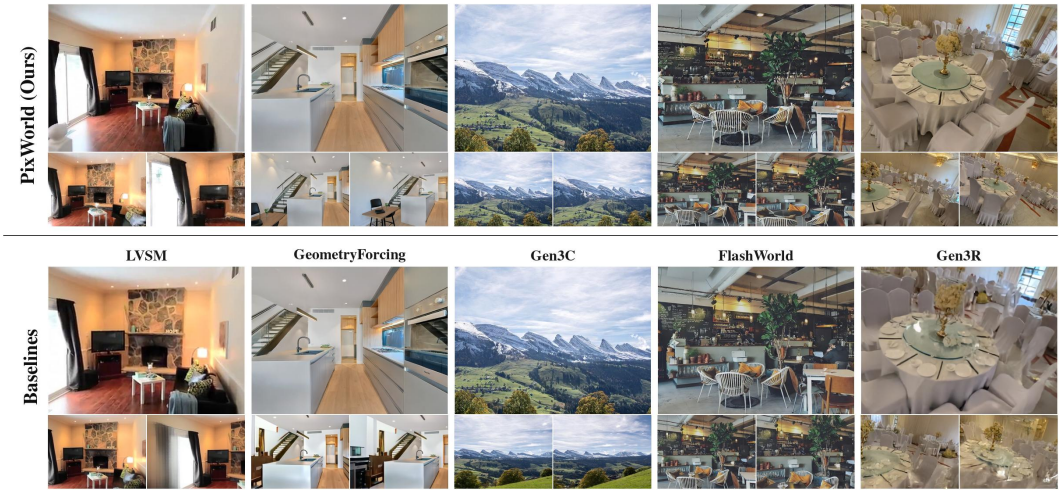

Figure 4: **Visualization of comparisons with baselines.** The large view on top denotes the input view, while the two smaller views below show novel views generated by each method.

loss supplies the 3D structural signal that 2D objectives cannot, validating it as a key component of PixWorld.

5 Conclusion

We present PixWorld, an end-to-end pixel-space diffusion framework that unifies 3D scene generation and reconstruction in a single model by partitioning multi-view inputs into clean and noisy subsets and producing a pixel-aligned 3D Gaussian representation in one forward pass. Eliminating the intermediate VAE/RAE stage avoids the information loss and extra training cost of latent autoencoders, and lets the diffusion objective directly supervise the 3D representation through differentiable rendering rather than an intermediate latent target; to further enforce 3D structural consistency beyond 2D photometric and perceptual losses, a geometry perception loss aligns rendered and ground-truth views in the geometry-aware feature space of a pretrained 3D foundation model. These results suggest that pixel-space diffusion, by removing latent indirection and naturally unifying generation with reconstruction, marks a promising paradigm toward scalable and unified 3D scene modeling.

References

Tianci Bi, Xiaoyi Zhang, Yan Lu, and Nanning Zheng. Vision foundation models can be good tokenizers for latent diffusion models. *arXiv preprint arXiv:2510.18457*, 2025.

David Charatan, Sizhe Lester Li, Andrea Tagliasacchi, and Vincent Sitzmann. pixelsplat: 3d gaussian splats from image pairs for scalable generalizable 3d reconstruction. In *Proceedings of the IEEE/CVF conference on computer vision and pattern recognition*, pp. 19457–19467, 2024.

Bowei Chen, Sai Bi, Hao Tan, He Zhang, Tianyuan Zhang, Zhengqi Li, Yuanjun Xiong, Jianming Zhang, and Kai Zhang. Aligning visual foundation encoders to tokenizers for diffusion models. *arXiv preprint arXiv:2509.25162*, 2025a.

Jiuhai Chen, Zhiyang Xu, Xichen Pan, Yushi Hu, Can Qin, Tom Goldstein, Lifu Huang, Tianyi Zhou, Saining Xie, Silvio Savarese, et al. Blip3-o: A family of fully open unified multimodal models-architecture, training and dataset. *arXiv preprint arXiv:2505.09568*, 2025b.

Shoufa Chen, Chongjian Ge, Shilong Zhang, Peize Sun, and Ping Luo. Pixelflow: Pixel-space generative models with flow. *arXiv preprint arXiv:2504.07963*, 2025c.

Yuedong Chen, Haofei Xu, Chuanxia Zheng, Bohan Zhuang, Marc Pollefeys, Andreas Geiger, Tat-Jen Cham, and Jianfei Cai. Mvsplat: Efficient 3d gaussian splatting from sparse multi-view images. In *European conference on computer vision*, pp. 370–386. Springer, 2024a.

Yuedong Chen, Chuanxia Zheng, Haofei Xu, Bohan Zhuang, Andrea Vedaldi, Tat-Jen Cham, and Jianfei Cai. Mvsplat360: Feed-forward 360 scene synthesis from sparse views. *Adv. Neural Inform. Process. Syst.*, 37:107064–107086, 2024b.

Zhennan Chen, Junwei Zhu, Xu Chen, Jiangning Zhang, Xiaobin Hu, Hanzhen Zhao, Chengjie Wang, Jian Yang, and Ying Tai. Dip: Taming diffusion models in pixel space. *arXiv preprint arXiv:2511.18822*, 2025d.

Jaeyoung Chung, Suyoung Lee, Hyeongjin Nam, Jaerin Lee, and Kyoung Mu Lee. Luciddreamer: Domain-free generation of 3d gaussian splatting scenes. *arXiv preprint arXiv:2311.13384*, 2023.

Yixiang Dai, Fan Jiang, Chiyu Wang, Mu Xu, and Yonggang Qi. Fantasyworld: Geometry-consistent world modeling via unified video and 3d prediction. *arXiv preprint arXiv:2509.21657*, 2025.

Prafulla Dhariwal and Alexander Nichol. Diffusion models beat gans on image synthesis. *Advances in neural information processing systems*, 34:8780–8794, 2021.

Jingtao Ding, Yunke Zhang, Yu Shang, Yuheng Zhang, Zefang Zong, Jie Feng, Yuan Yuan, Hongyuan Su, Nian Li, Nicholas Sukiennik, et al. Understanding world or predicting future? a comprehensive survey of world models. *ACM Computing Surveys*, 58(3):1–38, 2025.

Haoyi Duan, Hong-Xing Yu, Sirui Chen, Li Fei-Fei, and Jiajun Wu. Worldscore: A unified evaluation benchmark for world generation. *arXiv preprint arXiv:2504.00983*, 2025.

Patrick Esser, Sumith Kulal, Andreas Blattmann, Rahim Entezari, Jonas Müller, Harry Saini, Yam Levi, Dominik Lorenz, Axel Sauer, Frederic Boesel, et al. Scaling rectified flow transformers for high-resolution image synthesis. In *Int. Conf. Mach. Learn.*, 2024.

Rafail Fridman, Amit Abecasis, Yoni Kasten, and Tali Dekel. Scenescape: Text-driven consistent scene generation. *Adv. Neural Inform. Process. Syst.*, 36:39897–39914, 2023.

Ruiqi Gao, Aleksander Holynski, Philipp Henzler, Arthur Brussee, Ricardo Martin-Brualla, Pratul Srinivasan, Jonathan T Barron, and Ben Poole. Cat3d: Create anything in 3d with multi-view diffusion models. *arXiv preprint arXiv:2405.10314*, 2024.

Sensen Gao, Zhaoqing Wang, Qihang Cao, Dongdong Yu, Changhu Wang, Tongliang Liu, Mingming Gong, and Jiawang Bian. Oneworld: Taming scene generation with 3d unified representation autoencoder. *arXiv preprint arXiv:2603.16099*, 2026.

Hyojun Go, Dominik Narnhofer, Goutam Bhat, Prune Truong, Federico Tombari, and Konrad Schindler. Vist3a: Text-to-3d by stitching a multi-view reconstruction network to a video generator. *arXiv preprint arXiv:2510.13454*, 2025a.

Hyojun Go, Byeongjun Park, Jiho Jang, Jin-Young Kim, Soonwoo Kwon, and Changick Kim. Splatflow: Multi-view rectified flow model for 3d gaussian splatting synthesis. In *IEEE Conf. Comput. Vis. Pattern Recog.*, pp. 21524–21536, 2025b.

Hyojun Go, Byeongjun Park, Hyelin Nam, Byung-Hoon Kim, Hyungjin Chung, and Changick Kim. Videorfsplat: Direct scene-level text-to-3d gaussian splatting generation with flexible pose and multi-view joint modeling. *arXiv preprint arXiv:2503.15855*, 2025c.

Junlin Hao, Peiheng Wang, Haoyang Wang, Xinggong Zhang, and Zongming Guo. Gaussvideodreamer: 3d scene generation with video diffusion and inconsistency-aware gaussian splatting. *arXiv preprint arXiv:2504.10001*, 2025.

Yicong Hong, Kai Zhang, Jiuxiang Gu, Sai Bi, Yang Zhou, Difan Liu, Feng Liu, Kalyan Sunkavalli, Trung Bui, and Hao Tan. Lrm: Large reconstruction model for single image to 3d. *arXiv preprint arXiv:2311.04400*, 2023.

Emiel Hoogeboom, Jonathan Heek, and Tim Salimans. simple diffusion: End-to-end diffusion for high resolution images. In *International Conference on Machine Learning*, pp. 13213–13232. PMLR, 2023.

Emiel Hoogeboom, Thomas Mensink, Jonathan Heek, Kay Lamerigts, Ruiqi Gao, and Tim Salimans. Simpler diffusion: 1.5 fid on imagenet512 with pixel-space diffusion. In *Proceedings of the Computer Vision and Pattern Recognition Conference*, pp. 18062–18071, 2025.

Jiaxin Huang, Yuanbo Yang, Bangbang Yang, Lin Ma, Yuewen Ma, and Yiyi Liao. Gen3r: 3d scene generation meets feed-forward reconstruction. *arXiv preprint arXiv:2601.04090*, 2026.

Ziqi Huang, Yinan He, Jiashuo Yu, Fan Zhang, Chenyang Si, Yuming Jiang, Yuanhan Zhang, Tianxing Wu, Qingyang Jin, Nattapol Chanpaisit, et al. Vbench: Comprehensive benchmark suite for video generative models. In *IEEE Conf. Comput. Vis. Pattern Recog.*, pp. 21807–21818, 2024.

Allan Jabri, David J Fleet, and Ting Chen. Scalable adaptive computation for iterative generation. In *Proceedings of the 40th International Conference on Machine Learning*, pp. 14569–14589, 2023.

Wooseok Jang, Seonghu Jeon, Jisang Han, Jinhyeok Choi, Minkyung Kwon, Seungryong Kim, Saining Xie, and Sainan Liu. Repurposing geometric foundation models for multi-view diffusion. *arXiv preprint arXiv:2603.22275*, 2026.

Lihan Jiang, Yucheng Mao, Linning Xu, Tao Lu, Kerui Ren, Yichen Jin, Xudong Xu, Mulin Yu, Jiangmiao Pang, Feng Zhao, et al. Anysplat: Feed-forward 3d gaussian splatting from unconstrained views. *ACM Transactions on Graphics (TOG)*, 44(6):1–16, 2025.

Haian Jin, Hanwen Jiang, Hao Tan, Kai Zhang, Sai Bi, Tianyuan Zhang, Fujun Luan, Noah Snavely, and Zexiang Xu. Lvsm: A large view synthesis model with minimal 3d inductive bias. In *Int. Conf. Learn. Represent.*, 2025.

Bernhard Kerbl, Georgios Kopanas, Thomas Leimkühler, George Drettakis, et al. 3d gaussian splatting for real-time radiance field rendering. *ACM Trans. Graph.*, 42(4):139–1, 2023.

Diederik P Kingma and Max Welling. Auto-encoding variational bayes. *arXiv preprint arXiv:1312.6114*, 2013.

Lingdong Kong, Wesley Yang, Jianbiao Mei, Youquan Liu, Ao Liang, Dekai Zhu, Dongyue Lu, Wei Yin, Xiaotao Hu, Mingkai Jia, et al. 3d and 4d world modeling: A survey. *arXiv preprint arXiv:2509.07996*, 2025.

Haoyuan Li, Qihang Cao, Tao Tang, Kun Xiang, Zihan Guo, Jianhua Han, Jia-Wang Bian, Hang Xu, and Xiaodan Liang. Thinking with geometry: Active geometry integration for spatial reasoning. In *Proceedings of the 43rd International Conference on Machine Learning (ICML)*, Proceedings of Machine Learning Research. PMLR, 2026.

Ruilong Li, Brent Yi, Junchen Liu, Hang Gao, Yi Ma, and Angjoo Kanazawa. Cameras as relative positional encoding. *Advances in Neural Information Processing Systems*, 2025a.

Tianhong Li and Kaiming He. Back to basics: Let denoising generative models denoise. *arXiv preprint arXiv:2511.13720*, 2025.

Xinyang Li, Zhangyu Lai, Linning Xu, Yansong Qu, Liujuan Cao, Shengchuan Zhang, Bo Dai, and Rongrong Ji. Director3d: Real-world camera trajectory and 3d scene generation from text. *Adv. Neural Inform. Process. Syst.*, 37:75125–75151, 2024.

Xinyang Li, Tengfei Wang, Zixiao Gu, Shengchuan Zhang, Chunchao Guo, and Liujuan Cao. Flashworld: High-quality 3d scene generation within seconds. *arXiv preprint arXiv:2510.13678*, 2025b.

Xiuyu Li, Yijiang Liu, Long Lian, Huanrui Yang, Zhen Dong, Daniel Kang, Shanghang Zhang, and Kurt Keutzer. Q-diffusion: Quantizing diffusion models. In *Proceedings of the IEEE/CVF International Conference on Computer Vision*, pp. 17535–17545, 2023.

Chen-Hsuan Lin, Jun Gao, Luming Tang, Towaki Takikawa, Xiaohui Zeng, Xun Huang, Karsten Kreis, Sanja Fidler, Ming-Yu Liu, and Tsung-Yi Lin. Magic3d: High-resolution text-to-3d content creation. In *IEEE Conf. Comput. Vis. Pattern Recog.*, pp. 300–309, 2023.

Haotong Lin, Sili Chen, Junhao Liew, Donny Y Chen, Zhenyu Li, Guang Shi, Jiashi Feng, and Bingyi Kang. Depth anything 3: Recovering the visual space from any views. *arXiv preprint arXiv:2511.10647*, 2025.

Lu Ling, Yichen Sheng, Zhi Tu, Wentian Zhao, Cheng Xin, Kun Wan, Lantao Yu, Qianyu Guo, Zixun Yu, Yawen Lu, et al. Dl3dv-10k: A large-scale scene dataset for deep learning-based 3d vision. In *IEEE Conf. Comput. Vis. Pattern Recog.*, pp. 22160–22169, 2024.

Fangfu Liu, Wenqiang Sun, Hanyang Wang, Yikai Wang, Haowen Sun, Junliang Ye, Jun Zhang, and Yueqi Duan. Reconx: Reconstruct any scene from sparse views with video diffusion model. *arXiv preprint arXiv:2408.16767*, 2024.

Yuan Liu, Cheng Lin, Zijiao Zeng, Xiaoxiao Long, Lingjie Liu, Taku Komura, and Wenping Wang. Syncdreamer: Generating multiview-consistent images from a single-view image. *arXiv preprint arXiv:2309.03453*, 2023.

Ilya Loshchilov and Frank Hutter. Decoupled weight decay regularization. *arXiv preprint arXiv:1711.05101*, 2017.

Zehong Ma, Longhui Wei, Shuai Wang, Shiliang Zhang, and Qi Tian. Deco: Frequency-decoupled pixel diffusion for end-to-end image generation. *arXiv preprint arXiv:2511.19365*, 2025.

Ben Mildenhall, Pratul P Srinivasan, Matthew Tancik, Jonathan T Barron, Ravi Ramamoorthi, and Ren Ng. Nerf: Representing scenes as neural radiance fields for view synthesis. *Communications of the ACM*, 65(1):99–106, 2021.

William Peebles and Saining Xie. Scalable diffusion models with transformers. In *Int. Conf. Comput. Vis.*, pp. 4195–4205, 2023.

Dustin Podell, Zion English, Kyle Lacey, Andreas Blattmann, Tim Dockhorn, Jonas Müller, Joe Penna, and Robin Rombach. Sdxl: Improving latent diffusion models for high-resolution image synthesis. *arXiv preprint arXiv:2307.01952*, 2023.

Ben Poole, Ajay Jain, Jonathan T Barron, and Ben Mildenhall. Dreamfusion: Text-to-3d using 2d diffusion. *arXiv preprint arXiv:2209.14988*, 2022.

Xuanchi Ren, Tianchang Shen, Jiahui Huang, Huan Ling, Yifan Lu, Merlin Nimier-David, Thomas Müller, Alexander Keller, Sanja Fidler, and Jun Gao. Gen3c: 3d-informed world-consistent video generation with precise camera control. In *IEEE Conf. Comput. Vis. Pattern Recog.*, pp. 6121–6132, 2025.

Robin Rombach, Andreas Blattmann, Dominik Lorenz, Patrick Esser, and Björn Ommer. High-resolution image synthesis with latent diffusion models. In *IEEE Conf. Comput. Vis. Pattern Recog.*, pp. 10684–10695, 2022.

Kyle Sargent, Zizhang Li, Tanmay Shah, Charles Herrmann, Hong-Xing Yu, Yunzhi Zhang, Eric Ryan Chan, Dmitry Lagun, Li Fei-Fei, Deqing Sun, et al. Zeronvs: Zero-shot 360-degree view synthesis from a single real image. *arXiv preprint arXiv:2310.17994*, 2023.

Katja Schwarz, Denis Rozumny, Samuel Rota Bulò, Lorenzo Porzi, and Peter Kontschieder. A recipe for generating 3d worlds from a single image. In *Int. Conf. Comput. Vis.*, pp. 3520–3530, 2025.

Yuzhang Shang, Zhihang Yuan, Bin Xie, Bingzhe Wu, and Yan Yan. Post-training quantization on diffusion models. In *Proceedings of the IEEE/CVF conference on computer vision and pattern recognition*, pp. 1972–1981, 2023.

Noam Shazeer. Glu variants improve transformer. *arXiv preprint arXiv:2002.05202*, 2020.

Minglei Shi, Haolin Wang, Wenzhao Zheng, Ziyang Yuan, Xiaoshi Wu, Xintao Wang, Pengfei Wan, Jie Zhou, and Jiwen Lu. Latent diffusion model without variational autoencoder. *arXiv preprint arXiv:2510.15301*, 2025.

Yichun Shi, Peng Wang, Jianglong Ye, Mai Long, Kejie Li, and Xiao Yang. Mvdream: Multi-view diffusion for 3d generation. *arXiv preprint arXiv:2308.16512*, 2023.

Wenqiang Sun, Shuo Chen, Fangfu Liu, Zilong Chen, Yueqi Duan, Jun Zhang, and Yikai Wang. Dimensionx: Create any 3d and 4d scenes from a single image with controllable video diffusion. *arXiv preprint arXiv:2411.04928*, 2024.

Xiangyu Sun, Shijie Wang, Fengyi Zhang, Lin Liu, Caiyan Jia, Ziying Song, Zi Huang, and Yadan Luo. Vggt-world: Transforming vggt into an autoregressive geometry world model. *arXiv preprint arXiv:2603.12655*, 2026.

Stanislaw Szymanowicz, Chrisitian Rupprecht, and Andrea Vedaldi. Splatter image: Ultra-fast single-view 3d reconstruction. In *Proceedings of the IEEE/CVF conference on computer vision and pattern recognition*, pp. 10208–10217, 2024.

Jiaxiang Tang, Jiawei Ren, Hang Zhou, Ziwei Liu, and Gang Zeng. Dreamgaussian: Generative gaussian splatting for efficient 3d content creation. *arXiv preprint arXiv:2309.16653*, 2023.

Team Wan, Ang Wang, Baole Ai, Bin Wen, Chaojie Mao, Chen-Wei Xie, Di Chen, Feiwu Yu, Haiming Zhao, Jianxiao Yang, et al. Wan: Open and advanced large-scale video generative models. *arXiv preprint arXiv:2503.20314*, 2025.

Jianyuan Wang, Minghao Chen, Nikita Karaev, Andrea Vedaldi, Christian Rupprecht, and David Novotny. Vggt: Visual geometry grounded transformer. In *IEEE Conf. Comput. Vis. Pattern Recog.*, pp. 5294–5306, 2025a.

Jiepeng Wang, Zhaoqing Wang, Hao Pan, Yuan Liu, Dongdong Yu, Changhu Wang, and Wenping Wang. Mmgen: Unified multi-modal image generation and understanding in one go. *arXiv preprint arXiv:2503.20644*, 2025b.

Shuai Wang, Ziteng Gao, Chenhui Zhu, Weilin Huang, and Limin Wang. Pixnerd: Pixel neural field diffusion. *arXiv preprint arXiv:2507.23268*, 2025c.

Weijie Wang, Qihang Cao, Sensen Gao, Donny Y Chen, Haofei Xu, Wenjing Bian, Songyou Peng, Tat-Jen Cham, Chuanxia Zheng, Andreas Geiger, et al. Feed-forward 3d scene modeling: A problem-driven perspective. *arXiv preprint arXiv:2604.14025*, 2026.

Yifan Wang, Jianjun Zhou, Haoyi Zhu, Wenzheng Chang, Yang Zhou, Zizun Li, Junyi Chen, Jiangmiao Pang, Chunhua Shen, and Tong He. π^3: Permutation-equivariant visual geometry learning. *arXiv preprint arXiv:2507.13347*, 2025d.

Zhaoqing Wang, Xiaobo Xia, Zhuolin Bie, Jinlin Liu, Dongdong Yu, Jia-Wang Bian, and Changhu Wang. Taming camera-controlled video generation with verifiable geometry reward. *arXiv preprint arXiv:2512.02870*, 2025e.

Zhengyi Wang, Cheng Lu, Yikai Wang, Fan Bao, Chongxuan Li, Hang Su, and Jun Zhu. Prolificdreamer: High-fidelity and diverse text-to-3d generation with variational score distillation. *Adv. Neural Inform. Process. Syst.*, 36:8406–8441, 2023.

Zhou Wang, Alan C Bovik, Hamid R Sheikh, and Eero P Simoncelli. Image quality assessment: from error visibility to structural similarity. *IEEE transactions on image processing*, 13(4):600–612, 2004.

Haoyu Wu, Diankun Wu, Tianyu He, Junliang Guo, Yang Ye, Yueqi Duan, and Jiang Bian. Geometry forcing: Marrying video diffusion and 3d representation for consistent world modeling. *arXiv preprint arXiv:2507.07982*, 2025.

Rundi Wu, Ben Mildenhall, Philipp Henzler, Keunhong Park, Ruiqi Gao, Daniel Watson, Pratul P Srinivasan, Dor Verbin, Jonathan T Barron, Ben Poole, et al. Reconfusion: 3d reconstruction with diffusion priors. In *IEEE Conf. Comput. Vis. Pattern Recog.*, pp. 21551–21561, 2024.

Haofei Xu, Songyou Peng, Fangjinhua Wang, Hermann Blum, Daniel Barath, Andreas Geiger, and Marc Pollefeys. Depthsplat: Connecting gaussian splatting and depth. In *Proceedings of the Computer Vision and Pattern Recognition Conference*, pp. 16453–16463, 2025.

Yuanbo Yang, Jiahao Shao, Xinyang Li, Yujun Shen, Andreas Geiger, and Yiyi Liao. Prometheus: 3d-aware latent diffusion models for feed-forward text-to-3d scene generation. In *IEEE Conf. Comput. Vis. Pattern Recog.*, pp. 2857–2869, 2025.

Botao Ye, Boqi Chen, Haofei Xu, Daniel Barath, and Marc Pollefeys. Yonosplat: You only need one model for feedforward 3d gaussian splatting. In *International Conference on Learning Representations (ICLR)*, 2026a.

Seonghyeon Ye, Yunhao Ge, Kaiyuan Zheng, Shenyuan Gao, Sihyun Yu, George Kurian, Suneel Indupuru, You Liang Tan, Chuning Zhu, Jiannan Xiang, et al. World action models are zero-shot policies. *arXiv preprint arXiv:2602.15922*, 2026b.

Tianwei Yin, Michaël Gharbi, Taesung Park, Richard Zhang, Eli Shechtman, Fredo Durand, and William T Freeman. Improved distribution matching distillation for fast image synthesis. *Advances in neural information processing systems*, 37:47455–47487, 2024a.

Tianwei Yin, Michaël Gharbi, Richard Zhang, Eli Shechtman, Fredo Durand, William T Freeman, and Taesung Park. One-step diffusion with distribution matching distillation. In *Proceedings of the IEEE/CVF conference on computer vision and pattern recognition*, pp. 6613–6623, 2024b.

Hong-Xing Yu, Haoyi Duan, Junhwa Hur, Kyle Sargent, Michael Rubinstein, William T Freeman, Forrester Cole, Deqing Sun, Noah Snavely, Jiajun Wu, et al. Wonderjourney: Going from anywhere to everywhere. In *IEEE Conf. Comput. Vis. Pattern Recog.*, pp. 6658–6667, 2024.

Hong-Xing Yu, Haoyi Duan, Charles Herrmann, William T Freeman, and Jiajun Wu. Wonderworld: Interactive 3d scene generation from a single image. In *IEEE Conf. Comput. Vis. Pattern Recog.*, pp. 5916–5926, 2025a.

Yongsheng Yu, Wei Xiong, Weili Nie, Yichen Sheng, Shiqiu Liu, and Jiebo Luo. Pixeldit: Pixel diffusion transformers for image generation. *arXiv preprint arXiv:2511.20645*, 2025b.

Jiahui Zhang, Yuelei Li, Anpei Chen, Muyu Xu, Kunhao Liu, Jianyuan Wang, Xiao-Xiao Long, Hanxue Liang, Zexiang Xu, Hao Su, et al. Advances in feed-forward 3d reconstruction and view synthesis: A survey. *arXiv preprint arXiv:2507.14501*, 2025.

Lvmin Zhang, Anyi Rao, and Maneesh Agrawala. Adding conditional control to text-to-image diffusion models. In *Int. Conf. Comput. Vis.*, pp. 3836–3847, 2023.

Richard Zhang, Phillip Isola, Alexei A Efros, Eli Shechtman, and Oliver Wang. The unreasonable effectiveness of deep features as a perceptual metric. In *IEEE Conf. Comput. Vis. Pattern Recog.*, pp. 586–595, 2018.

Yuyang Zhao, Chung-Ching Lin, Kevin Lin, Zhiwen Yan, Linjie Li, Zhengyuan Yang, Jianfeng Wang, Gim Hee Lee, and Lijuan Wang. Genxd: Generating any 3d and 4d scenes. *arXiv preprint arXiv:2411.02319*, 2024.

Boyang Zheng, Nanye Ma, Shengbang Tong, and Saining Xie. Diffusion transformers with representation autoencoders. *arXiv preprint arXiv:2510.11690*, 2025.

Tinghui Zhou, Richard Tucker, John Flynn, Graham Fyffe, and Noah Snavely. Stereo magnification: learning view synthesis using multiplane images. *ACM Trans. Graph.*, 37(4):1–12, 2018.

Yang Zhou, Hao Shao, Letian Wang, Zhuofan Zong, Hongsheng Li, and Steven L Waslander. Drivinggen: A comprehensive benchmark for generative video world models in autonomous driving. *arXiv preprint arXiv:2601.01528*, 2026.

A Overview of the Appendix

This appendix supplements the main paper along five axes. Appendix B details the architecture of the two-stream MMDiT denoiser with a per-component parameter budget, together with the data, batching, and optimization recipes used to train PixWorld from scratch. Appendix C provides disaggregated quantitative results on 1-view and 2-view generation, separating the configurations averaged in the main paper to reveal how each method behaves on the harder versus easier side of each setting. Appendix D presents additional qualitative visualizations covering reconstruction and generation under diverse view selections, with both RGB renderings and predicted depth maps. Appendix E reports an inference-speed comparison against representative baselines. Finally, the responsible-considerations (Appendix F) section discusses limitations, broader impacts, and LLM usage.

B Implementation Details

Architecture. PixWorld's denoiser f_θ is a 24-layer DiT (Peebles & Xie, 2023) with hidden width d=1024, 16 attention heads (head dim 64), SwiGLU (Shazeer, 2020) feed-forward layers, RMSNorm on Q, K, and adaLN-Zero modulation conditioned on the diffusion timestep. Following the SD3-style MMDiT (Esser et al., 2024) design, each block hosts two parallel streams that share topology but maintain independent pre-LayerNorm, QKV / output projections, MLP, and adaLN-Zero weights: a clean stream processes the conditioning views in Ω_c, and a noise stream processes the noisy views in Ω_n. Inside the attention operator, the per-stream Q, K, V tensors are concatenated along the token axis (with shared q, k-RMSNorm) and a single full attention is computed jointly over $[\,\Omega_\mathrm{c};\,\Omega_\mathrm{n}\,]$, so conditioning and noisy tokens cross-talk in every layer; the joint output is then split back and routed through stream-specific output projections. The two streams share a single cross-attention to text tokens and a single timestep embedder, the latter evaluated at t=1 for the clean stream and at the sampled t for the noise stream, allowing one model to serve both pose-only and text-conditioned generation. Camera parameters are injected via PRoPE (Li et al., 2025a). Inputs use a 16×16 patchify with learnable positional embeddings, and the final layer emits per-pixel depth and 3D-Gaussian attributes through stream-specific multi-task heads, with Gaussian centers obtained by unprojecting each pixel using its predicted depth (Sec. 3.2). The total trainable parameter count is 1.044 B; Table 6 reports the per-component budget.

Data and batching. The RealEstate10K (Zhou et al., 2018) and DL3DV-10K (Ling et al., 2024) datasets together provide $\sim$67K posed multi-view scenes. From each scene we sample $N \in \{4, \ldots, 8\}$ views and partition them into $\Omega_\mathrm{c}/\Omega_\mathrm{n}$, biasing the sampler toward small $|\Omega_\mathrm{c}|$ so capacity is spent on conditioned generation. We additionally mix in a single-image branch of 10M images drawn from the BLIP-3o (Chen et al., 2025b) corpus, which shares the diffusion backbone and strengthens the 2D appearance prior. On each GPU, every optimization step alternates a 32-image single-view batch with a multi-view batch of up to 32 images (*e.g.*, 4–8 views $\times$ 4–8 scenes).

Optimization. We optimize $\mathcal{L} = \mathcal{L}_\mathrm{render} + \lambda_\mathrm{depth}\,\mathcal{L}_\mathrm{depth} + \lambda_\mathrm{geo}\,\mathcal{L}_\mathrm{geo}$ with λ_depth=1.0 and λ_lpips=λ_geo=0.1, gating $\mathcal{L}_\mathrm{lpips}$ and $\mathcal{L}_\mathrm{geo}$ at t>t_th=0.3 since perceptual and geometric supervision is unreliable when the noisy input is close to pure noise. The frozen geometry critic Ψ is instantiated as π^3 (Wang et al., 2025d), with gradients stopped on the reference branch. Training is run from scratch (no image- or video-model pretraining) using AdamW (Loshchilov & Hutter, 2017) with a linearly decayed learning rate from 1×10^{-4} to 1×10^{-5}, EMA decay 0.9995, gradient clipping at 1.0, and classifier-free text dropping at rate 0.2. Training runs for $\sim$200K steps on 32 NVIDIA A800-SXM4-80G GPUs.

C Detailed Results on 1-View and 2-View Generation

The main paper (Tab. 2 and Tab. 3) reports numbers averaged within each input setting to keep the comparison compact. For completeness, we provide the disaggregated per-configuration results here. Under the 1-view setting, the average is taken over two complementary configurations: First Frame, where the input view is the first frame of the clip and the model generates a purely forward trajectory along a long, fully extrapolative horizon; and Bidirectional, where a randomly chosen middle frame

Table 6: **Architecture of the two-stream DiT denoiser f_θ.** Each block follows an MMDiT-style design: the clean and noise streams maintain independent pre-LayerNorm, QKV / output projections, SwiGLU MLP, and adaLN-Zero weights, while a single full attention is computed jointly over the concatenated $[\,\Omega_{\mathrm{c}};\,\Omega_{\mathrm{n}}\,]$ tokens with shared q, k-RMSNorm. The cross-attention to text and the timestep embedder are also shared across streams, and output heads are duplicated per stream so that both clean and noisy tokens are decoded into depth and 3D-Gaussian attributes at every patch.

Module	Configuration	#Params
(a) Tokenization & conditioning		
Clean-view patch embed	16×16 patchify, $3\to1024$	0.79 M
Noisy-view patch embed	16×16 patchify, $3\to1024$	0.79 M
Positional embedding	learnable, 588×1024	0.60 M
Timestep embedder	sinusoidal 256 + MLP $1024\to1024$	1.31 M
Text projection	MLP $4096\to1024\to1024$	5.24 M
(b) Two-stream MMDiT block ($\times$ 24; d=1024, h=16, d_h=64)		
QKV projection (clean)	pre-LN + $1024\to3\times1024$	3.15 M
Output projection (clean)	$1024\to1024$	1.05 M
SwiGLU MLP (clean)	$1024\to2\times2730\to1024$	8.39 M
adaLN-Zero (clean)	t-cond. γ, β, α ($\times6$)	6.30 M
QKV projection (noise)	pre-LN + $1024\to3\times1024$	3.15 M
Output projection (noise)	$1024\to1024$	1.05 M
SwiGLU MLP (noise)	$1024\to2\times2730\to1024$	8.39 M
adaLN-Zero (noise)	t-cond. γ, β, α ($\times6$)	6.30 M
Joint full attention	SDPA over $[\Omega_{\mathrm{c}};\Omega_{\mathrm{n}}]$ with shared q, k-RMSNorm	~ 0
Cross-attention to text	shared by both streams	4.20 M
	per-block subtotal	41.98 M
	trunk total ($\times$24 blocks)	1007.6 M
(c) Multi-task output heads (duplicated per stream)		
Depth head	adaLN + linear $1024\to16\times16\times1$	$2\times$2.36 M
3D-Gaussian head	adaLN + linear $1024\to16\times16\times35$	$2\times$11.28 M
Total trainable parameters		1.044 B

conditions generation toward both ends, producing two shorter and roughly symmetric horizons that more directly test local consistency around the input. Under the 2-view setting, the average is taken over Interpolation, where the two anchors bracket the target trajectory and the model fills in intermediate views, and Extrapolation, where both anchors lie at one end of the clip and the model must generate views beyond their span under stronger parallax. The disaggregated results in Tab. 7 and Tab. 8 reveal two consistent trends. First, every method degrades on the harder side of each setting (First Frame for 1-view, Extrapolation for 2-view), with the largest gaps appearing on LPIPS and on the Camera Control AUC@$\{30^\circ, 15^\circ, 5^\circ\}$ metrics. Second, the method ranking is largely preserved across configurations, confirming that the averaged numbers in the main paper faithfully summarize each method's behavior rather than being dominated by the easier sub-configuration. PixWorld remains the top performer on nearly every column across all four configurations, with the largest margins precisely on the harder sides, indicating that our design generalizes best in the extrapolation- and parallax-heavy regimes where competing methods suffer most.

D Additional Visualizations

We provide additional qualitative results to complement the quantitative comparisons in the main paper. Fig. 6 shows reconstruction and generation across diverse view selections: for each scene, we visualize the camera trajectory with input views and generated views marked, alongside the RGB renderings and the depth maps predicted by PixWorld. These examples cover varied input counts and trajectory shapes, and demonstrate that PixWorld produces geometrically coherent scenes regardless of how the input views are arranged. Fig. 7 further showcases generated scenes from a single input view (shown as the first frame of each sequence), with both RGB renderings and the corresponding depth maps. Across these examples, the predicted depth remains sharp and structurally consistent

Table 7: **Quantitative comparison on single-image 3D scene generation, per configuration.** We evaluate on RealEstate10K (Zhou et al., 2018) and DL3DV-10K (Ling et al., 2024) under 1-view First Frame and 1-view Bidirectional. Best in **bold**; second best underlined.

	Novel View Synthesis			*Generation Quality*				*Camera Control*		
Method	PSNR↑	SSIM↑	LPIPS↓	I2V Subj.↑	I2V BG↑	I.Q.↑	Aes.Q.↑	AUC@30↑	AUC@15↑	AUC@5↑
RealEstate10K – 1-view First Frame										
LVSM (Jin et al., 2025)	17.95	0.604	0.335	0.968	0.971	0.584	0.505	0.695	0.576	0.359
GF (Wu et al., 2025)	15.92	0.575	0.436	0.942	0.947	0.514	0.487	0.609	0.488	0.301
Gen3C (Ren et al., 2025)	17.12	0.622	0.394	0.959	0.961	0.569	0.530	0.664	0.521	0.338
FlashWorld (Li et al., 2025b)	16.26	0.613	0.417	0.951	0.954	**0.617**	0.544	0.849	0.766	0.553
Gen3R (Huang et al., 2026)	17.43	0.628	0.383	0.973	0.970	0.547	0.531	0.653	0.443	0.145
PixWorld (Ours)	**18.92**	**0.683**	**0.324**	**0.977**	**0.979**	0.608	**0.549**	**0.872**	**0.804**	**0.621**
RealEstate10K – 1-view Bidirectional										
LVSM (Jin et al., 2025)	17.70	0.601	0.337	0.974	0.969	0.603	0.506	0.726	0.608	0.385
GF (Wu et al., 2025)	15.34	0.532	0.471	0.921	0.935	0.495	0.462	0.583	0.467	0.279
Gen3C (Ren et al., 2025)	17.39	0.626	0.388	0.943	0.952	0.553	0.517	0.632	0.507	0.329
FlashWorld (Li et al., 2025b)	16.75	0.639	0.390	0.966	0.967	0.614	0.555	0.837	0.751	0.539
Gen3R (Huang et al., 2026)	17.74	0.633	0.381	0.975	0.972	0.557	0.541	0.612	0.424	0.150
PixWorld (Ours)	**18.83**	**0.721**	**0.325**	**0.981**	**0.978**	**0.639**	**0.563**	**0.865**	**0.793**	**0.607**
DL3DV-10K – 1-view First Frame										
LVSM (Jin et al., 2025)	14.85	0.434	0.533	0.927	0.932	0.491	0.463	0.537	0.354	0.127
GF (Wu et al., 2025)	12.50	0.352	0.598	0.894	0.907	0.468	0.431	0.482	0.329	0.109
Gen3C (Ren et al., 2025)	15.72	0.516	0.482	0.925	0.928	0.526	0.491	0.556	0.371	0.121
FlashWorld (Li et al., 2025b)	15.31	0.468	0.463	0.939	0.950	0.616	0.558	0.765	0.667	0.412
Gen3R (Huang et al., 2026)	15.57	0.499	0.504	0.941	0.940	0.543	0.529	0.614	0.408	0.102
PixWorld (Ours)	**16.37**	**0.521**	**0.455**	**0.947**	**0.953**	**0.624**	**0.564**	**0.789**	**0.702**	**0.477**
DL3DV-10K – 1-view Bidirectional										
LVSM (Jin et al., 2025)	14.96	0.432	0.526	0.934	0.933	0.497	0.468	0.568	0.391	0.141
GF (Wu et al., 2025)	12.88	0.361	0.584	0.902	0.913	0.479	0.439	0.501	0.346	0.118
Gen3C (Ren et al., 2025)	15.44	0.512	0.476	0.929	0.937	0.537	0.501	0.548	0.382	0.134
FlashWorld (Li et al., 2025b)	15.53	0.478	0.458	0.944	0.950	0.621	0.559	0.773	0.681	0.428
Gen3R (Huang et al., 2026)	15.94	0.507	0.487	0.948	0.944	0.551	0.532	0.571	0.389	0.133
PixWorld (Ours)	**16.63**	**0.533**	**0.443**	**0.956**	**0.958**	**0.637**	**0.571**	**0.797**	**0.709**	**0.493**

with the rendered appearance, indicating that the joint depth and 3D-Gaussian prediction in PixWorld captures scene geometry faithfully even under heavy extrapolation from a single conditioning image. Finally, Fig. 5 complements our ablation study by qualitatively comparing PixWorld with and without the Geometry Perception loss, where the full model yields sharper later-view renderings and more accurate pose control. Beyond these on-page visualizations, we further provide video comparisons of 3D scenes generated by different methods in the supplementary zip file, where the camera pose of each rendered video is additionally estimated to quantitatively assess camera control precision.

E Inference Speed Comparison

We benchmark inference speed on a single NVIDIA A100-SXM4-80G GPU in Tab. 9, reporting wall-clock time per scene, the number of key frames, and the number of function evaluations (NFE). PixWorld generates a scene in 15 seconds, reaching the same order of magnitude as the highly optimized FlashWorld (10 s). We note that this comparison is not strictly apples-to-apples: PixWorld currently runs at a lower output resolution than the video-diffusion baselines, which reduces per-step compute. More fundamentally, PixWorld does not rely on video-model priors and thus does not need to materialize a dense frame sequence: a 3D representation is reconstructed from as few as 8 key frames, after which novel views are rendered efficiently via differentiable rasterization. By contrast, video-diffusion pipelines denoise a long frame sequence end-to-end, with Gen3C, Gen3R, and FlashWorld producing 121, 49, and 24 frames per scene, respectively. Note also that PixWorld and Gen3R use a comparable NFE (100), while FlashWorld leverages distillation to reduce its NFE to 4, which largely accounts for its strong runtime. We view distillation as complementary to our approach: the numbers above are for the base, undistilled PixWorld, and combining it with distillation (Yin et al., 2024b;a) and post-training quantization (Li et al., 2023; Shang et al., 2023) is a natural next step (see Appendix F.1).

Table 8: **Quantitative comparison on two-view 3D scene generation, per configuration.** We evaluate on RealEstate10K (Zhou et al., 2018) and DL3DV-10K (Ling et al., 2024) under 2-view Interpolation and 2-view Extrapolation. Best in **bold**; second best underlined.

	Novel View Synthesis			*Generation Quality*				*Camera Control*		
Method	PSNR↑	SSIM↑	LPIPS↓	I2V Subj.↑	I2V BG↑	I.Q.↑	Aes.Q.↑	AUC@30↑	AUC@15↑	AUC@5↑
RealEstate10K – 2-view Interpolation										
LVSM (Jin et al., 2025)	**24.26**	**0.832**	**0.200**	0.969	0.963	0.613	0.518	0.871	0.806	0.638
GF (Wu et al., 2025)	18.08	0.621	0.373	0.936	0.951	0.525	0.476	0.642	0.487	0.236
Gen3C (Ren et al., 2025)	20.17	0.726	0.298	0.967	0.949	0.581	0.527	0.714	0.553	0.261
FlashWorld (Li et al., 2025b)	21.66	0.776	0.252	0.958	0.959	0.619	0.546	0.875	0.810	0.634
Gen3R (Huang et al., 2026)	22.42	0.752	0.260	0.964	0.973	0.544	0.539	0.779	0.631	0.295
PixWorld (Ours)	23.44	0.810	0.214	**0.971**	**0.975**	**0.625**	**0.559**	**0.877**	**0.814**	**0.648**
RealEstate10K – 2-view Extrapolation										
LVSM (Jin et al., 2025)	22.95	0.806	0.230	0.972	0.965	0.601	0.514	0.851	0.771	0.583
GF (Wu et al., 2025)	18.46	0.672	0.332	0.914	0.927	0.489	0.451	0.618	0.458	0.211
Gen3C (Ren et al., 2025)	20.08	0.703	0.302	0.928	0.945	0.552	0.509	0.682	0.524	0.249
FlashWorld (Li et al., 2025b)	21.30	0.765	0.261	0.970	0.965	0.618	0.548	0.878	0.813	0.640
Gen3R (Huang et al., 2026)	20.24	0.695	0.307	0.976	0.970	0.556	0.542	0.677	0.521	0.220
PixWorld (Ours)	**23.63**	**0.819**	**0.206**	**0.978**	**0.974**	**0.631**	**0.564**	**0.883**	**0.819**	**0.651**
DL3DV-10K – 2-view Interpolation										
LVSM (Jin et al., 2025)	**19.37**	**0.594**	**0.328**	0.918	0.917	0.538	0.511	0.758	0.630	0.403
GF (Wu et al., 2025)	15.16	0.452	0.480	0.903	0.918	0.487	0.452	0.573	0.395	0.156
Gen3C (Ren et al., 2025)	17.81	0.546	0.406	0.931	0.938	0.541	0.508	0.641	0.446	0.183
FlashWorld (Li et al., 2025b)	18.16	0.559	0.363	0.937	0.951	0.602	0.564	0.812	0.724	0.528
Gen3R (Huang et al., 2026)	18.21	0.562	0.391	0.940	0.946	0.531	0.536	0.745	0.582	0.260
PixWorld (Ours)	19.12	0.581	0.348	**0.953**	**0.957**	**0.611**	**0.568**	**0.826**	**0.739**	**0.542**
DL3DV-10K – 2-view Extrapolation										
LVSM (Jin et al., 2025)	18.98	0.584	0.358	0.913	0.916	0.528	0.493	0.723	0.587	0.346
GF (Wu et al., 2025)	15.61	0.466	0.459	0.891	0.906	0.471	0.438	0.553	0.362	0.137
Gen3C (Ren et al., 2025)	17.42	0.539	0.418	0.924	0.930	0.532	0.496	0.614	0.421	0.169
FlashWorld (Li et al., 2025b)	18.37	0.565	0.356	0.938	0.946	0.598	0.552	0.793	0.703	0.501
Gen3R (Huang et al., 2026)	17.88	0.554	0.392	0.943	0.941	0.539	0.523	0.706	0.538	0.231
PixWorld (Ours)	**19.61**	**0.607**	**0.331**	**0.947**	**0.954**	**0.604**	**0.561**	**0.817**	**0.728**	**0.526**

Table 9: **Inference speed comparison** on a single NVIDIA A100-SXM4-80G GPU. We report the wall-clock time to generate one scene, the number of key frames per scene, and the number of function evaluations (NFE).

Method	#Key Frames per scene	NFE	Time per scene (s) ↓
Gen3C (Ren et al., 2025)	121	70	791
Gen3R (Huang et al., 2026)	49	100	882
FlashWorld (Li et al., 2025b)	24	4	**10**
PixWorld (Ours)	8	100	15

F Responsible Considerations

F.1 Limitations.

PixWorld takes a step toward unifying 3D scene reconstruction and generation in pixel space, but several directions remain open. Our experiments focus on widely used scene-level datasets such as RealEstate10K and DL3DV-10K; further evaluation on more diverse outdoor and object-centric scenes would better characterize the framework's generalization. Pixel-space diffusion with differentiable rendering is also trained under finite resolution and compute budgets, leaving room for improvements in fine-grained texture fidelity and scalability to higher-resolution multi-view settings. Finally, we plan to accelerate PixWorld's inference through distillation (Yin et al., 2024b;a) and quantization (Li et al., 2023; Shang et al., 2023), further reducing the cost of high-quality 3D scene generation.

F.2 Broader impacts.

PixWorld may benefit applications such as efficient 3D reconstruction, 3D content creation, robotic perception, simulation, and VR/AR. At the same time, improved 3D scene reconstruction and genera-

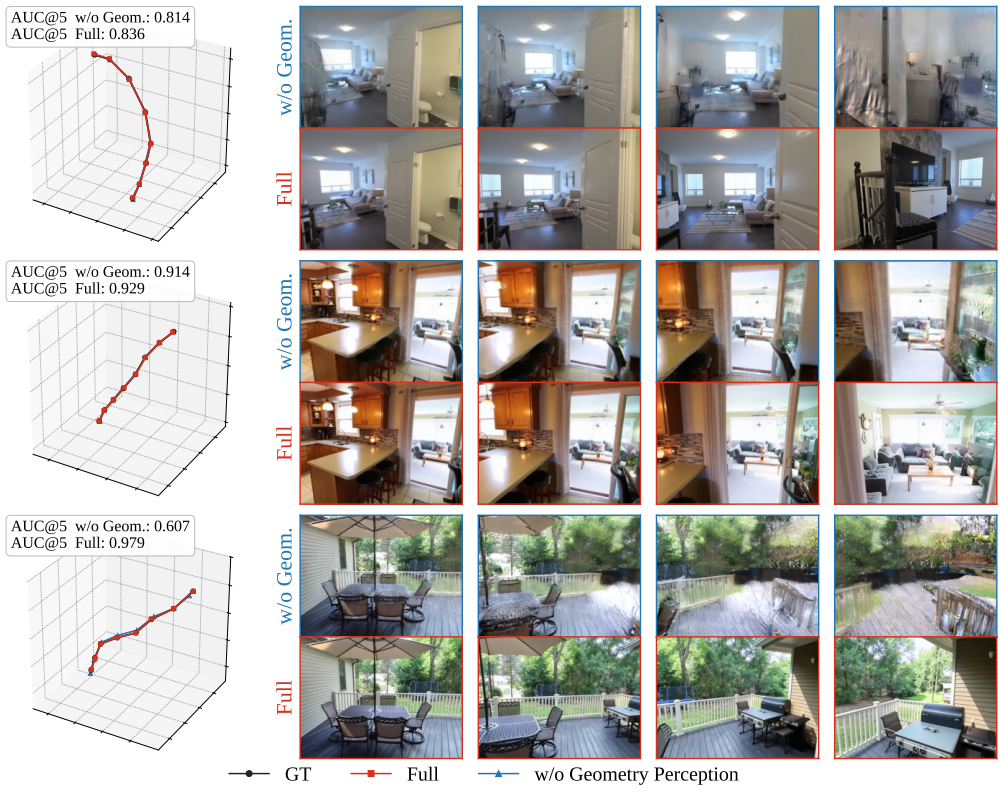

Figure 5: **Ablation study on the Geometry Perception loss in PixWorld.** Given a single input image, our model generates the subsequent 7 frames (8 frames in total); we visualize 4 representative frames here for clarity. Pose accuracy is quantitatively evaluated by comparing the estimated camera poses against the ground-truth poses. Compared to the variant without Geometry Perception (*w/o Geom.*), the full model achieves more precise camera pose control and substantially mitigates the blurriness in later-view predictions, demonstrating that the global 3D perception loss is essential for maintaining both geometric consistency and visual fidelity over long generation horizons.

tion may raise concerns about privacy-sensitive scene capture, misuse of synthetic or reconstructed 3D content, and unreliable deployment in safety-critical settings. We encourage responsible data usage, careful evaluation, and human oversight when applying such systems in real-world scenarios.

F.3 LLM USAGE.

This work does not use LLMs as an important, original, or non-standard component of the core method. Any use of LLM-based tools, if any, was limited to writing, editing, or formatting assistance and did not affect the methodology, experiments, or scientific conclusions.

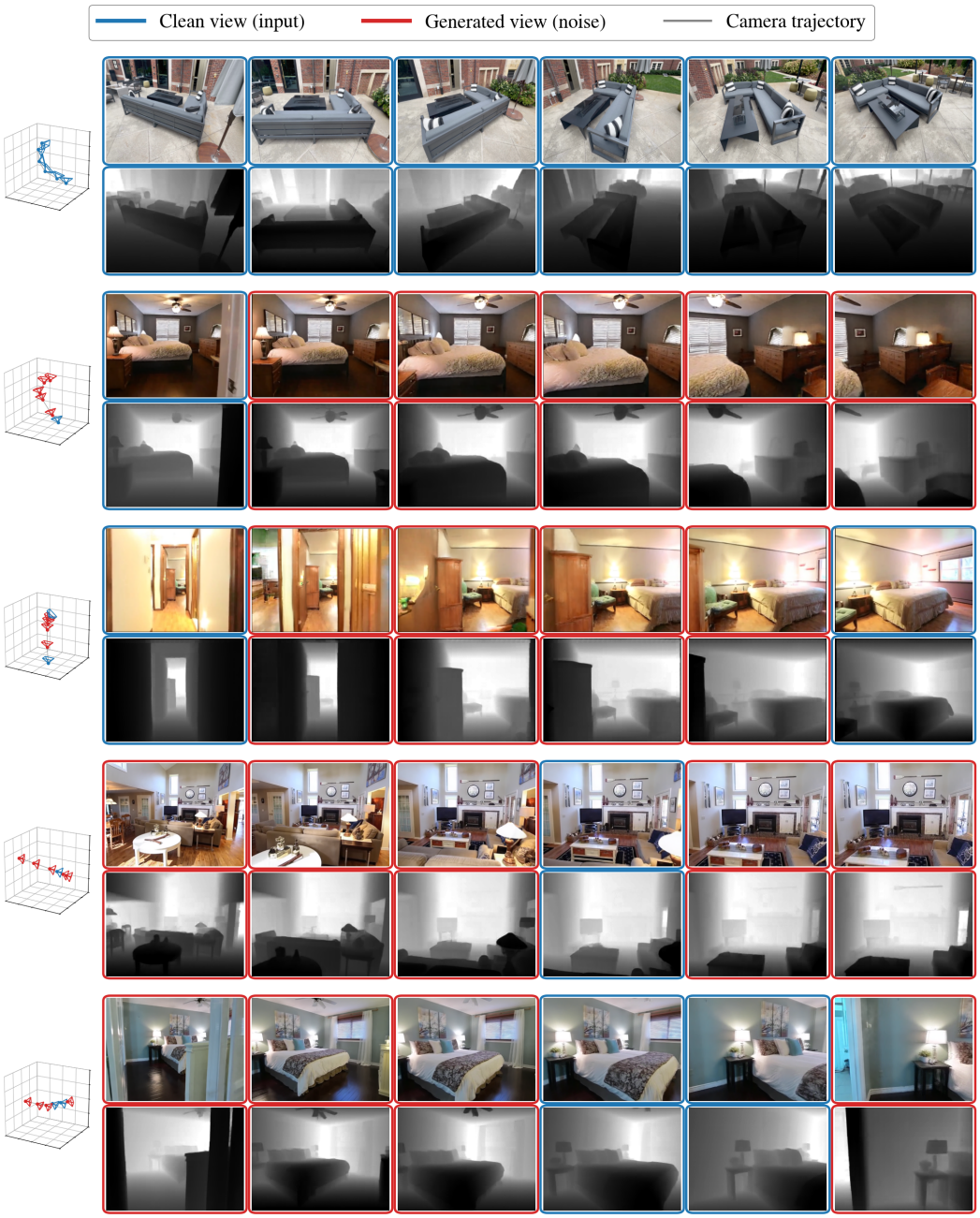

Figure 6: More visualizations of reconstruction and generation under varying view selections, including camera trajectories with input and generated views marked, and the corresponding depth maps predicted by PixWorld.

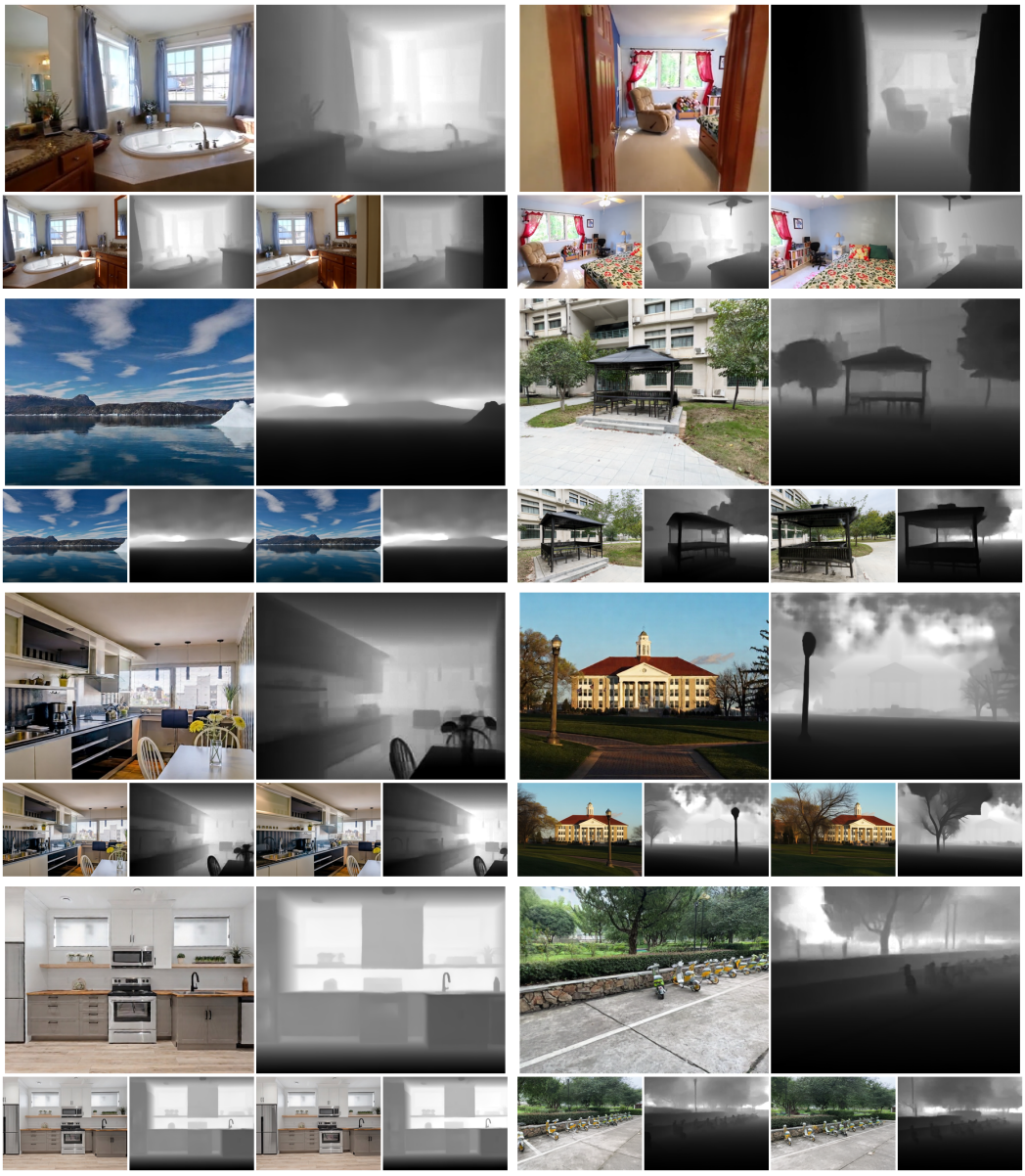

Figure 7: More visualizations of generated scenes. The first view is the input, and we show both RGB renderings and predicted depth maps.